buildings

MDPI

Article

Design and Wind-Induced Fatigue Analysis of a Dynamic Movable Sculpture in Coastal Environments: A Case Study of the Welcome Tower

Leming Gu [1,*], Haixia Liu [1], Mingzhuo Rui [1], Laizhu Jiang [2], Jie Chen [3], Dagen Dong [4], Hai Wang [5] and Jianguo Cai [6]

[1] East China Architecture Design & Research Institute Co., Ltd., Shanghai 200002, China
[2] Tsingtuo Group Co., Ltd., Fu'an 355006, China
[3] China Construction First Group Co., Ltd., Beijing 100161, China
[4] Shanghai Redesign Landscape Engineering Co., Ltd., Shanghai 201700, China
[5] Shanghai AGAPE Electromechanical Tech Co., Ltd., Shanghai 201907, China
[6] School of Civil Engneering, Southeast University, Nanjing 211102, China
* Correspondence: glm17369@ecadi.com

Abstract

This study focuses on the design, material selection, and wind-induced fatigue analysis of a dynamic movable sculpture atop the Welcome Tower at Yazhou Bay Bougainvillea Park in Sanya. The sculpture, consisting of eight movable leaves, is driven by a hydraulic system enabling it to assume five distinct shapes. Nickel-saving stainless steel (S22152/S32001) was chosen as the primary material due to its excellent corrosion resistance and strength, ensuring durability in the harsh coastal environment. The mechanical system is designed with a two-level lifting device, rotation system, and push-rod mechanism, allowing the leaves to perform functions such as rising, opening, closing, and rotating while minimizing mechanical load. Wind tunnel tests and numerical simulations were conducted to analyze the sculpture's performance under wind loads. Using the rain-flow counting method and Miner's linear fatigue accumulation theory, the study calculated stress amplitude and fatigue damage, finding that the most unfavorable fatigue life of the sculpture's components is 380 years. This analysis demonstrates that the sculpture will not experience fatigue damage over its expected lifespan, providing valuable insights for the design of dynamic sculptures in coastal environments. The research integrates mechanical design, material selection, and fatigue analysis, ensuring the sculpture's long-term stability and resistance to wind-induced fatigue.

Keywords: movable sculpture; mechanical device; nickel-saving stainless steel; embodied carbon

Check for updates

Academic Editor: Gabriele Milani

Received: 9 November 2025
Revised: 9 December 2025
Accepted: 19 December 2025
Published: 14 January 2026

Copyright: © 2026 by the authors. Licensee MDPI, Basel, Switzerland. This article is an open access article distributed under the terms and conditions of the Creative Commons Attribution (CC BY) license.

1. Introduction

As global climate change increasingly affects building design and structural performance, coastal buildings face numerous challenges, particularly regarding wind loads [1], corrosive environments [2], and structural durability [3]. Wind loads not only threaten the stability and safety of buildings but also contribute to wind-induced fatigue, impacting long-term performance [4]. Therefore, selecting appropriate building materials [5] and design solutions [6] is crucial for structures located in coastal areas. This is especially true for dynamic structures like movable sculptures, where wind-induced fatigue significantly affects their shape changes and structural stability [7,8].

Traditional building materials, particularly carbon steel, are prone to rapid deterioration in marine environments due to their inadequate corrosion resistance [9]. The aggressive nature of saltwater, coupled with high humidity and fluctuating temperatures, accelerates the corrosion process, undermining the structural integrity and long-term functionality of carbon steel [10]. In coastal regions, where structures are consistently exposed to harsh environmental conditions, including saline mist and extreme weather events, the degradation of carbon steel is notably accelerated [11]. This leads to increased maintenance requirements, elevated costs, and potential safety risks. Consequently, the use of carbon steel in such settings has become increasingly untenable due to its relatively short lifespan and the high cost of maintenance, rendering it an impractical solution for coastal construction [12].

To mitigate these challenges, stainless steel, particularly nickel-saving stainless steel, has emerged as the preferred material in coastal building design due to its superior corrosion resistance, mechanical strength, and cost-effectiveness over the lifecycle of the structure [13]. Stainless steel's ability to withstand the corrosive effects of saltwater and other harsh environmental factors is due to the formation of a passive chromium oxide layer that protects the material from further oxidation [14]. This makes it an ideal choice for coastal structures exposed to continuous and severe marine conditions. Notably, nickel-saving stainless steel grades, such as S22152, offer enhanced corrosion resistance, higher tensile strength, and excellent resistance to localized corrosion, such as pitting and crevice corrosion, all while reducing dependence on costly nickel [14–16]. The incorporation of elements like nitrogen and molybdenum, instead of nickel, enhances the material's performance while simultaneously reducing material costs, making it a more economically viable option compared to conventional stainless steel grades [17]. Furthermore, stainless steel's superior weldability ensures strong, durable joints, crucial for maintaining the structural integrity of large-scale coastal installations [18]. Therefore, the combination of durability, cost efficiency, and fabrication versatility positions nickel-saving stainless steel as the material of choice for sustainable and reliable coastal construction projects.

Despite the widespread recognition of stainless steel's corrosion resistance, the impact of wind-induced fatigue on stainless steel structures remains an important research topic [19]. Under wind load, dynamic structures such as the leaves of movable sculptures often experience significant cyclic loading [20–22]. This cyclic loading can lead to material fatigue, ultimately affecting the structural safety and functionality [23]. As a new material, nickel-saving stainless steel S22152 has not been fully studied in the context of wind-induced fatigue, particularly in its performance in real-world engineering applications.

This study focuses on the dynamic sculpture atop the Welcome Tower at Yazhou Bay in Sanya, with an emphasis on the sculpture's design, material selection, and wind-induced fatigue performance. By utilizing stainless steel materials and incorporating advanced mechanical drive systems, the sculpture achieves a perfect balance between stability under wind loads and dynamic aesthetics. The study conducts detailed wind-induced fatigue damage assessments through wind tunnel testing, numerical simulations, and fatigue analysis, providing an effective design framework and theoretical support for similar future projects.

2. Movable Sculpture Design

2.1. Project Information

Yazhou Bay Bougainvillea Park is situated approximately 2.5 km from the South China Sea coastline in Sanya City. The Welcome Tower, located at the center of the park, is the highest point of the entire project. The project location and real-world images are shown in Figure 1.

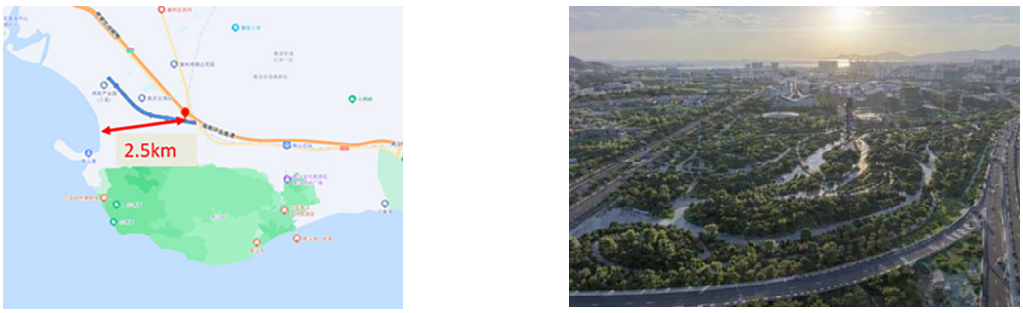

(**a**) Project location (**b**) Real photos of the project

Figure 1. Project location and real scene photos.

As shown in Figure 2, the flower crown atop the Welcome Tower is a dynamic sculpture driven by mechanical systems. It consists of eight movable leaves, each covered with a silver PTFE mesh membrane. To reflect the themes of Yazhou City, five distinct shapes were designed: "Breaking through the Soil", "Colorful Flower", "Rice Field and Wheat Waves", "Hope Torch", and "Dragon Entering the Sea". Under normal conditions, the leaves remain in a folded state.



Figure 2. The five state shapes of the flower crown of the welcome tower in Bougainvillea park.

The city experiences strong winds. The 50-year basic wind pressure in Sanya is 0.85 kPa, and the ground roughness is classified as Class B. Wind load values were determined through wind tunnel testing [24]. During normal operation, the tower cannot function when the wind speed at the top exceeds 17.45 m/s (the upper limit of Beaufort scale level 6). If the average wind speed at the top exceeds 17.45 m/s (maximum wind speed of Beaufort scale level 6), the system will shut down, and the leaves will be adjusted to the folded position.

2.2. Fixed Scheme for Dynamic Sculpture at the Top of the Welcome Tower

As shown in Figure 3, the Welcome Tower stands at a height of 48 m, with its top corolla composed of eight leaves and mechanical devices. These devices enable the sculpture to transform into various shapes. In the "Hope Torch" state, the height reaches 74 m. The tower features a triangular grid tube structure, with a transfer level positioned at an elevation of 35 m to transfer the corolla's weight to the foundation via an elevator tube. At the 39 m elevation, an extension arm truss is incorporated to utilize the grid tube structure in resisting the overturning moment of the corolla under wind load.

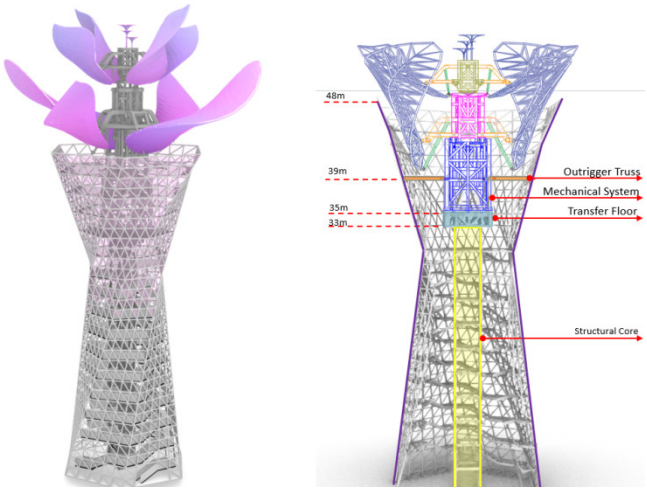

Figure 3. Fixed scheme of the corolla structure at the top of the welcome tower.

2.3. Mechanical Scheme

To achieve five distinct corolla shapes, the leaves must perform functions such as rising, opening and closing, and rotating. Therefore, the mechanical system is divided into two levels: the first-level lifting device and the second-level lifting device. These two levels can independently control the rotation and movement of the leaves.

As shown in Figure 4, at the bottom of the mechanical device is a first-stage fixed cylinder, within which a first-stage lifting structure is housed, with a rotating disc positioned above the lifting structure. Similarly, a secondary fixed cylinder is placed above the turntable, housing a secondary lifting structure, with a secondary turntable positioned above it. A three-stage fixed cylinder is located above the two-stage rotating turntable. The lower large leaf is fixed to the second fixed cylinder, while the upper small leaf is attached to the third fixed cylinder.

Thus, the first lifting structure and the first rotating disc drive the lifting and rotation of the large lower leaf, while the secondary lifting structure and secondary turntable control the movement of the smaller leaves in the upper layer. This mechanical system includes a hydraulic drive unit, a slider and track system, a rotation system, a safety pin system, and an electrical control system.

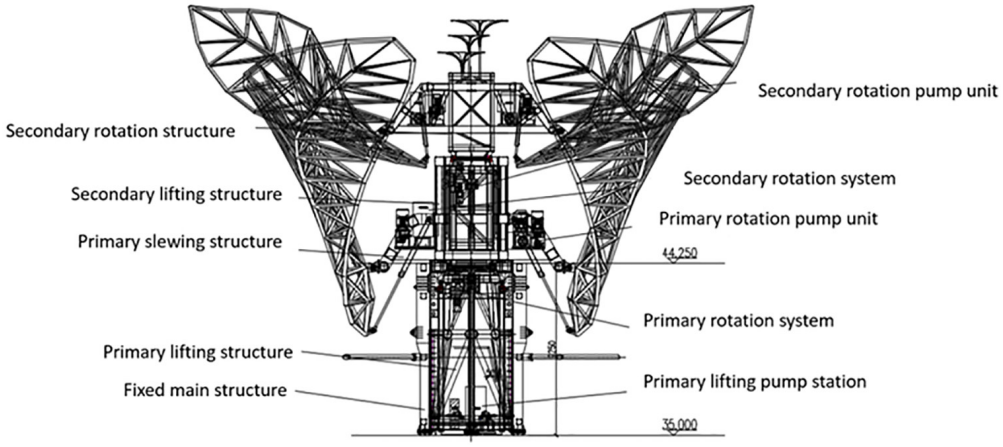

Figure 4. Schematic diagram of the mechanical device.

2.3.1. Lifting System and Rotating System

A hydraulic push rod is positioned between the fixed cylinder and the internal lifting structure, enabling the structure to ascend and descend. A track is placed on the inner side

of the fixed cylinder, and the lifting structure contacts the track through MEG engineering plastic sliders. Once the structure reaches the target position, it is secured and fixed by an electric pin (bolt). The lifting rate is 1 m/min, with the first hydraulic push rod having a limit of 7 m and the second push rod limited to 3 m. Schematic diagrams of the system are shown in Figures 5 and 6.

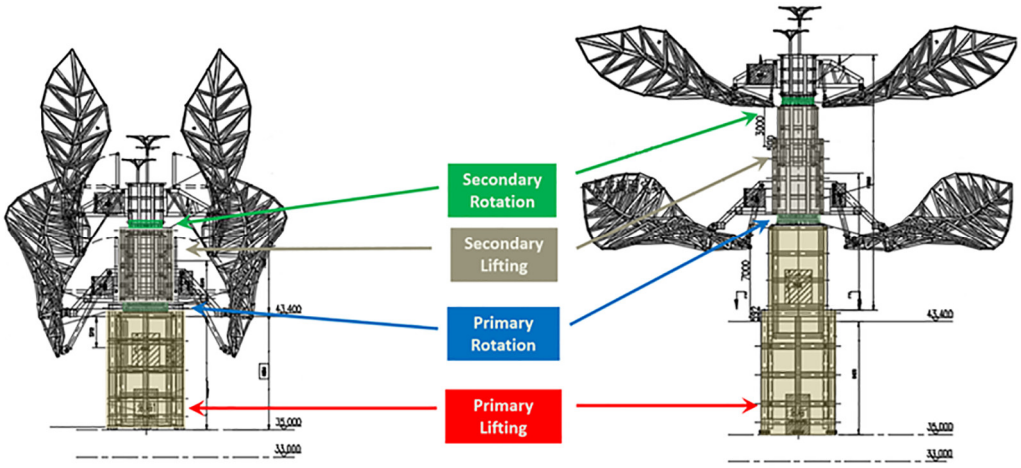

Figure 5. Diagram of leaf lifting and rotation.

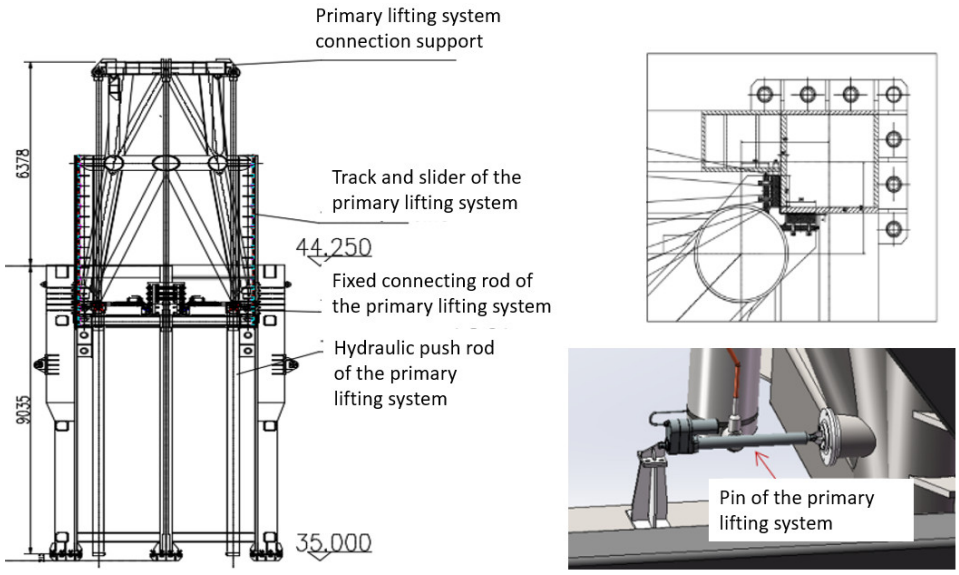

Figure 6. Schematic diagram of the first-stage lift system.

As shown in Figure 7, the first-stage rotation of the mechanical device is primarily driven by the first-stage rotation motor, which engages a gear to mesh with the slewing bearing. The slewing bearing is connected to both the first-stage lifting structure and the first-stage rotation structure, enabling the rotation of the entire mechanical sculpture device. To ensure safe rotation when the device is not in operation, an electric pin system is incorporated. When inactive, the structure is positioned and locked by the rotating pin. The rotation angle ranges from 0° to 350°, with a rotation speed of 0.3 r/min.

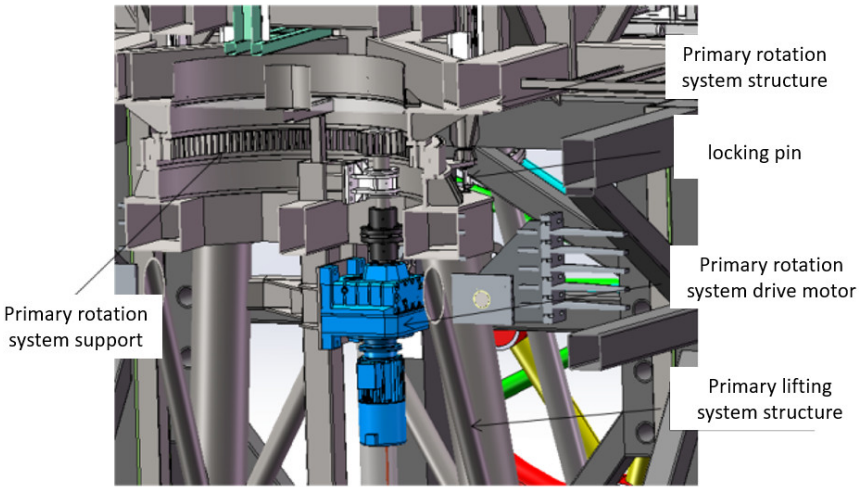

Figure 7. Rotating system of the mechanical device.

2.3.2. Leaf Opening and Closing System

There are two common methods for opening and closing the leaves: The first is the torque drive scheme, which offers the advantage of a smaller drive unit but suffers from low structural redundancy and challenges in handling the rigid connection between the leaf root and the drive unit. The second method is the push rod scheme, which has the advantage of hinged connections for both the leaf structure and the transmission device. This design provides a longer force arm at the leaf root, which helps resist overturning under wind loads, but its mechanical connections are more complex. Both schemes are illustrated in Figure 8. In summary, the torque drive scheme is more suitable for small machinery, while the push rod scheme is better suited for the large-scale sculpture in this project.

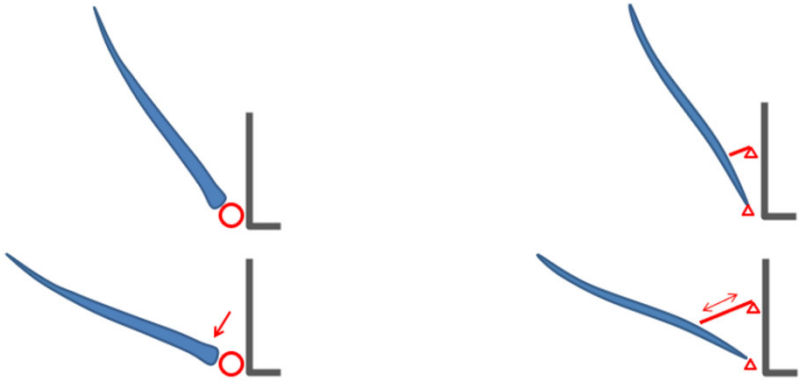

(**a**) Torque scheme (**b**) Push rod scheme

Figure 8. Two drive schemes for leaf opening and closing.

To securely fasten the leaf structure to the mechanical device, at least three points must extend from the device to constrain the leaf. Given that the leaf shape is wider in the middle and narrower at the ends, only one constraint point can be placed at the bottom of the leaf, as indicated by the red dot in Figure 9. To minimize interference from the connecting components, the other two constraint points are positioned in the lower middle section of the leaf structure, as shown by the blue dots in Figure 9.

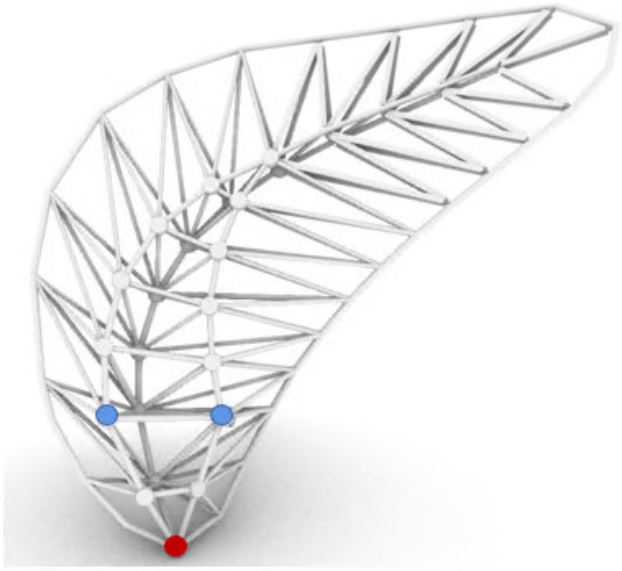

Figure 9. Constraint points of the mechanical device on the leaf.

Based on the conditions outlined above, two push rods must be positioned to connect to the blue points on the leaf structure shown in Figure 9. The synchronization requirements for the push rods when the leaf is both opened and closed are quite strict. To simplify the drive system, the adjustment mechanism will actuate the push rod at the red point, with the blue point serving as the fixed connection point.

The push rods must be positioned as vertically as possible relative to the leaf to maximize the efficiency of force transmission. If a horizontal push rod is used, its efficiency is significantly reduced when the leaf is open. Additionally, the maximum limit of the push rod is determined by its length when fully retracted. Therefore, the connection node on the mechanical device should be moved upwards, as shown in Figure 10.

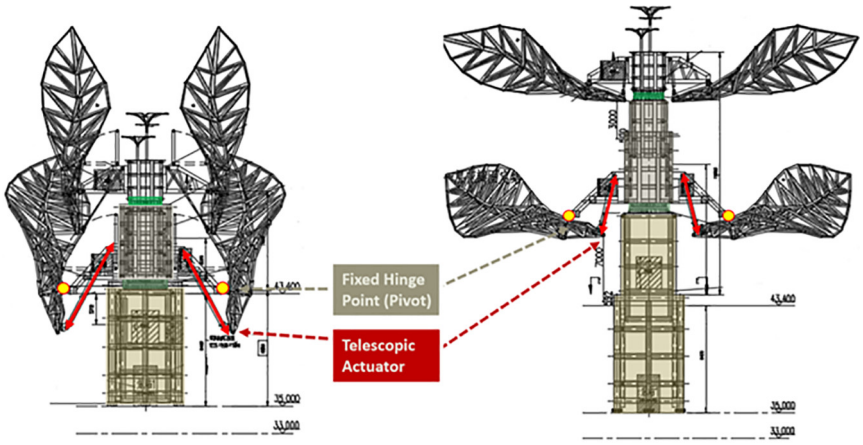

Figure 10. Diagram of the leaf opening.

Another issue with the push rod setup is that while the leaf can withstand the maximum wind load when retracted, the angle between the push rod and the leaf structure becomes small, reducing the efficiency of wind load resistance. To address this, horizontal safety rods and pin devices are added in the retracted position to help resist wind loads. In this state, the safety rods must be lowered, while the upper and lower locking devices secure the lower node of the leaf structure, as shown in Figure 11.

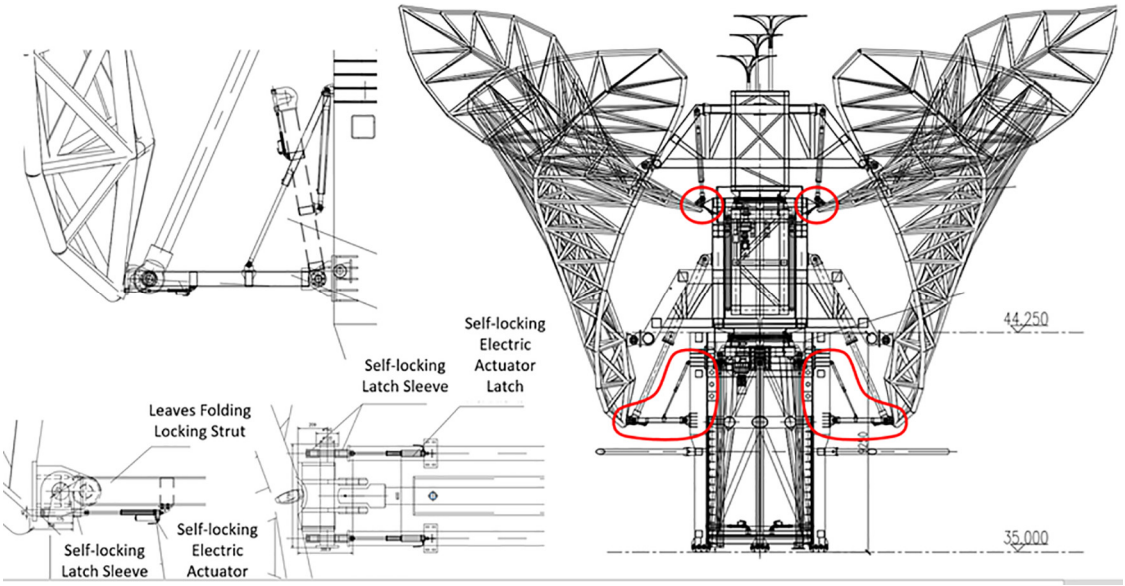

Figure 11. Horizontal safety rods and pin devices in the folded state.

The parameters of the mechanical device in the folded state, along with the five different corolla shapes, are shown in the Table 1. In the folded state, the upper small leaves are opened to 60° to minimize their windward area.

Table 1. Working parameters for each state.

	Folded Status	Breaking the Soil	Colorful Flower	Rice Field and Wheat Waves	Hope Torch	Dragon Entering the Sea
One lift	—	7 m	7 m	7 m	7 m	7 m
Second lift	—	—	1.5 m	1 m	3 m	—
First rotation	—	—	—	45°	—	—
Secondary rotation	—	45°	45°	45°	—	45°
Small leaf opening Angle	—	—	45°	70°	30°	70°
Large leaf opening Angle	60°	—	50°	70 °	—	20°

Note: The opening angles are all angles with the vertical plane.

3. Leaf Structures Scheme

As shown in Figures 12 and 13, the sculpture consists of a total of 8 leaves, with the lower 4 being larger and the upper 4 smaller. The movement trajectories of the leaves and collision detection were simulated using Autodesk Revit software.

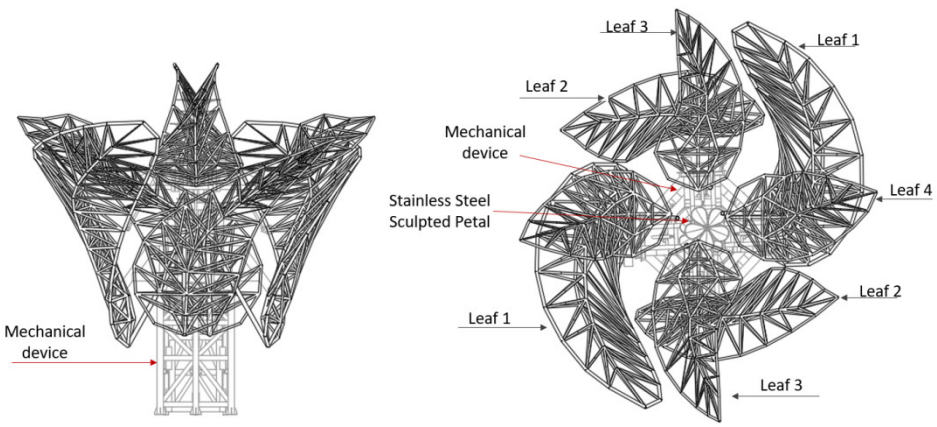

Figure 12. Elevation and plan views of the leaf in the folded state.

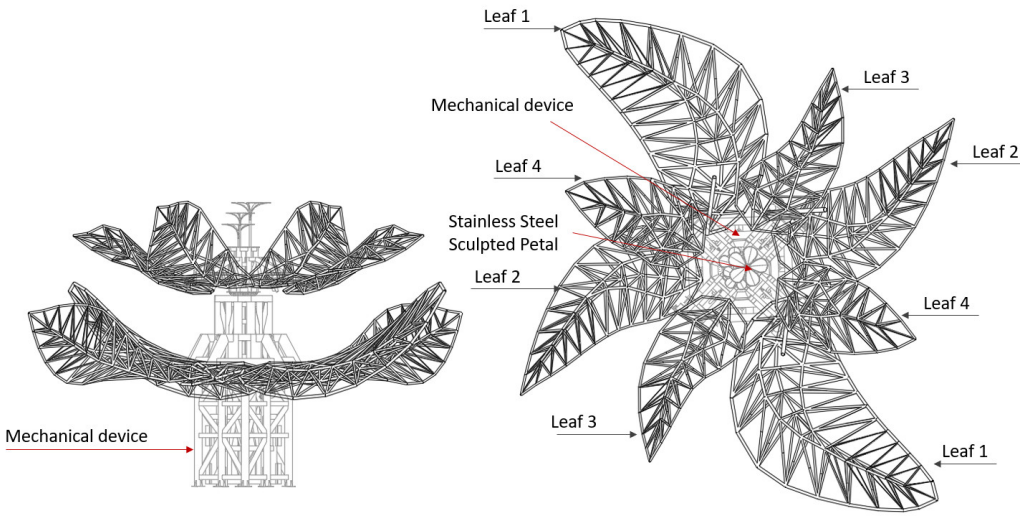

Figure 13. Elevation and plan views of the leaf in the open state.

The design of the leaf structure has two key differences compared to ordinary building structures: First, the leaf structures are mechanically driven and must be as lightweight as possible to reduce the mechanical load. Second, they are situated in an open coastal environment, subject to harsh corrosive conditions.

3.1. Leaf Structure

As shown in Figure 14, The leaf features a spatial grid structure, with a triangular core at the center and trusses suspending the sides to form its outer profile. At the tip of the leaf, an I-shaped solid web section is used for the overhanging member due to space constraints.

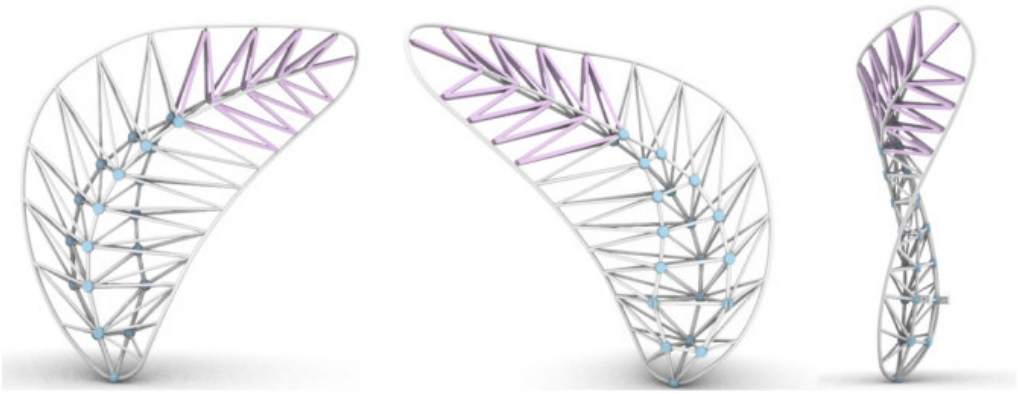

Figure 14. Diagram of the leaf structure.

The core area of the leaf contains numerous intersecting nodes, using truncated spherical nodes. The edge nodes have fewer intersecting members, and intersecting nodes are used in these areas, as shown in Figure 15.

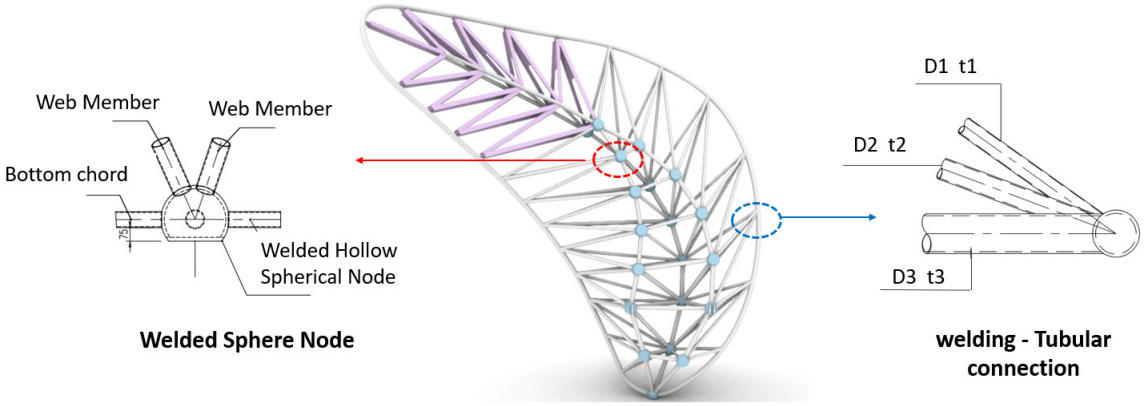

Figure 15. Schematic diagram of the leaf structure node.

3.2. Structure Material

The sculpture is located outdoors near the coastline, where it is exposed to harsh corrosive conditions. Due to the limited interior space of the leaf, it is impossible to set up a walkway for maintenance. Therefore, ensuring the durability of the leaf structure is crucial.

Three material options were considered: Option 1 involves using aluminum alloy, which is lightweight and has good corrosion resistance. However, its strength significantly decreases after welding, making it unsuitable for wind resistance requirements. Additionally, mechanical connection nodes have poor adaptability to the irregular spatial structure of the project. Option 2 uses ordinary steel with a coating, which is easy to construct but lacks durability, as the coating degrades over time. Option 3 involves stainless steel, which offers both construction convenience and durability but is more expensive. Therefore, nickel-saving stainless steel (S22152/S32001) was selected. This type of stainless steel reduces the nickel content and increases the proportion of other alloys, thereby reducing costs while maintaining strength and corrosion resistance. The pitting corrosion rate of this material is approximately 7.82 g/(mh^2), comparable to that of conventional 304 austenitic stainless steel (Cr18Ni8 type). Thus, stainless steel (S22152/S32001) was chosen as the material for the leaf structure. The chemical composition and mechanical properties of this stainless steel are presented in Tables 2 and 3.

Table 2. Chemical Composition Table (Melting Analysis/%).

		C	Si	Mn	P	S	Cr	Ni	N
Limits	min			4.0			19.50	1.00	0.05
	max	0.030	1.00	6.00	0.040	0.030	21.5	3.00	0.17
Test determination		0.024	0.36	4.10	0.035	0.001	21.25	1.62	0.12

Table 3. Mechanical properties.

	Ultimate Tensile Strength fu	Nominal Yield Strength f0.2	Elongation After Fracture A (%)	Shock Absorption Energy (KV2/J)
Limits	≥620	≥450	≥25	—
Base material test determination	662	466	33	Room temperature 72 0 degrees 61
Post-weld test determination	Base material fracture	—	—	—

Note: The specimen size for the impact toughness test is 55 × 10 × 5 mm.

3.3. Economy and Embodied Carbon Emissions Consideration

We also compared the economic costs and embodied carbon emissions of stainless steel and coated steel. Although stainless steel has a higher initial cost during construction, its lower maintenance frequency and longer service life lead to reduced total cost and embodied carbon emissions over the entire lifecycle. Therefore, the use of stainless steel offers better long-term economic and environmental performance. Finally, we chose stainless steel as the structure material of leaves.

4. Wind-Induced Fatigue Damage Calculation

4.1. Wind Tunnel Test Overview

The rigid model pressure wind tunnel test was performed at the TJ-2 Atmospheric Boundary Layer Wind Tunnel Laboratory of the Civil Engineering Disaster Prevention and Mitigation National Key Laboratory at Tongji University. Due to the large size of the model, the lower third of the tower was removed to avoid significantly affecting the overall flow characteristics. The blockage ratio during the wind tunnel test was maintained below 5%, with a calculated value of approximately 3.75%. The geometric scale ratio was 1:50, and the time scale ratio was 1:12.25. The experimental model is shown in Figure 16.



(**a**) Wind Tunnel Layout and Model Appearance (**b**) Wind pressure measurement point

Figure 16. Wind tunnel test model.

The silver PTFE mesh membrane covering the leaf surfaces primarily serves decorative and protective purposes. In the 1:50-scale wind-tunnel model, solid surfaces were used instead of perforated membranes to ensure reliable pressure measurements. Although the actual porosity of the membrane was not determined, it may slightly reduce mean and fluctuating pressure coefficients. Therefore, adopting solid surfaces represents a conservative assumption, ensuring that the design wind loads and fatigue analysis reflect the upper-bound aerodynamic condition.

The far-field terrain analysis was performed using topographic and land-use data within a 5 km radius of the site, obtained from GIS and satellite imagery, supplemented by on-site photographs. The analysis identified the surroundings as a coastal urban zone with low- to medium-density buildings and vegetation, corresponding to Class B wind field. The measured wind speed and turbulence intensity profiles during the test were compared with the specifications [3], where the roughness of the Class B terrain was taken as 0.15, as shown in Figure 17a. In this comparison, z represents the relative height of the test point (i.e., the actual height divided by 2.5 m), U is the measured wind speed at height z, I_u is the turbulence intensity at the test point, and U_{ref} is the reference wind speed measured at the reference point. The reference point denotes the location at the reference height (z_ref) used for measuring the reference wind speed (U_ref) in the atmospheric boundary-layer

flow. The reference height corresponds to the top of the simulated boundary layer in the wind-tunnel test.

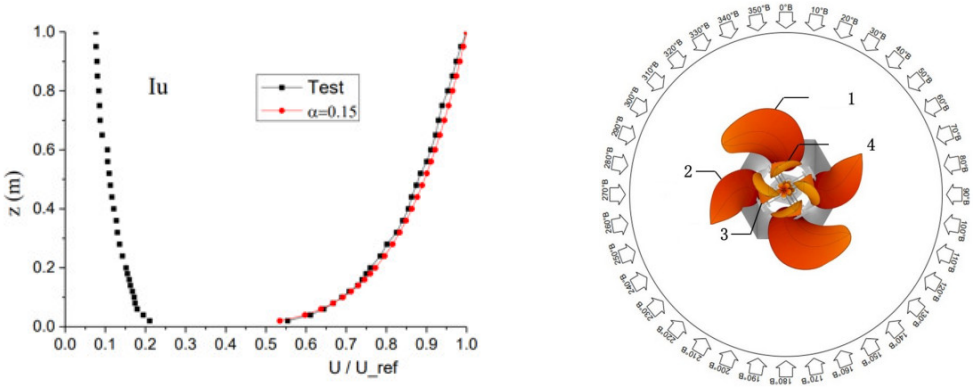

(**a**) Inflow Wind Profile (**b**) Definition of Wind Direction

Figure 17. Wind tunnel test layout and operating conditions.

Considering the design standards and testing equipment, the wind tunnel test was conducted with an actual wind speed of 37.25 m/s and a wind speed scale ratio of 1:4.08. The range of wind direction angles was from 0° to 350°, with intervals of 10°, resulting in a total of 36 wind direction angles. The specified 0° wind direction is shown in Figure 17b. In the subsequent calculations, the wind pressure coefficient time histories at the leaf measurement points under the 36 different wind direction conditions were extracted as input data for the structural stress analysis of the wind load.

It should be noted that the 0° wind direction in the wind tunnel test differs by 152° from the 0° wind direction in the meteorological data. When numerically integrating the joint probability density function of wind speed and wind direction, the wind direction angle range for integration was determined based on the wind direction conditions observed in the wind tunnel test.

4.2. Fatigue Stress Amplitude

In the wind tunnel test, a total of 15,000 data points were recorded at each test point. These data were converted using the time scale ratio to match the wind pressure time history for a 10 min duration in the actual engineering scenario. To optimize computational efficiency, only 1500 data points were selected, corresponding to 1 min of pressure measurement data. An equidistant sampling method was then applied, extracting 300 wind pressure data points from the wind tunnel test to serve as the wind load input, with a time step of 0.2 s.

The basic wind pressure w_0 used in the wind tunnel test was selected based on the 50-year recurrence period for Sanya City, with a value of 0.85 kPa. A total of 36 conditions were calculated based on the experimental setup. The measured wind pressure coefficients were averaged in blocks and converted into surface loads applied to the leaf surfaces. For leaf 1, the calculation model is shown in Figure 18, where the positions and numbers of some rods are indicated.

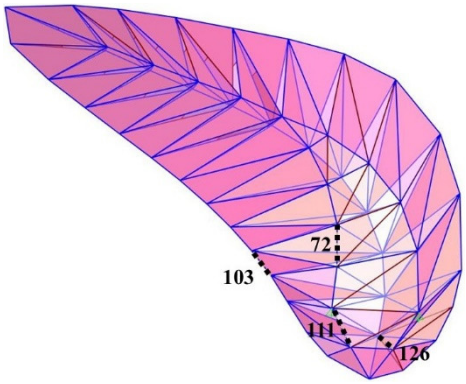

Figure 18. Analysis model diagram of leaf 1 and number of members.

The stress time history of the internal stainless steel tubes in the leaves was calculated using SAP 2000. In the SAP 2000 analysis, the root of the leaf was fully fixed to simulate the rigid connection with the mechanical device, while the rods were modeled as pin-connected truss members. The wind pressure time histories obtained from the wind tunnel test were converted into equivalent surface loads and applied to the leaf panels. When the wind speed reached 24 m/s, the maximum instantaneous stress (106 MPa) occurred at the end node of rod 103 on leaf 1, while the maximum stress amplitude, obtained from the stress-time-history analysis, was 132 MPa at the end node of rod 111. Both conditions occurred on leaf 1, which was therefore selected to represent the entire structure in the fatigue-life analysis. Following the maximum stress principle, four critical rods were selected for fatigue analysis: rods 72, 103, 111, and 126. The stress time histories at the nodes of these rods were extracted for further analysis.

Finite element calculations using ABAQUS revealed that the maximum stress at the ball joints, where multiple rods are connected, was approximately 1.5 times greater than the maximum stress in the individual rods. As a result, the stress in the rods was amplified by a factor of 1.5, and the fatigue life of the ball joints was verified. Stress amplitude and mean stress were calculated using the rain-flow counting method [25].

The basic steps of the rain-flow counting method are as follows: First, the time history data is processed by retaining only the peak and valley values. Next, four consecutive values are extracted in time order, and the difference between the second and third values is compared with the difference between the first and fourth values. If the difference between the second and third values is greater than or equal to the difference between the first and fourth, the average of the second and third values is taken as the mean stress for one stress cycle, and their difference is the stress amplitude for that cycle. The second and third values are then removed from the load time history, and the process is repeated for the next four values. If the difference between the second and third values is smaller than the difference between the first and fourth, the first value is retained, and the next four values are extracted in order, corresponding to values 2, 3, 4, and 5. The process is repeated for all values. Finally, all stress amplitudes and mean stresses from the second step are summarized, and the frequency of each combination of stress amplitude and mean stress is counted. This method is known as the "four-point" rain-flow counting method.

For example, for rod 111, under a 350° wind direction and a wind speed of 23 m/s, its stress time history is shown in Figure 19. The stress amplitude, mean stress, and number of stress cycles for this condition, calculated using the rain-flow counting method, are shown in Figure 20 and used for subsequent fatigue calculations.

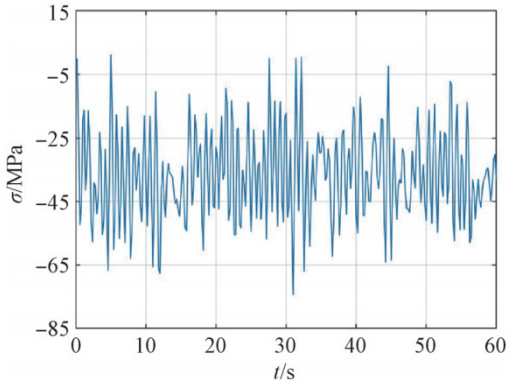

Figure 19. Stress time history at node of member 111.

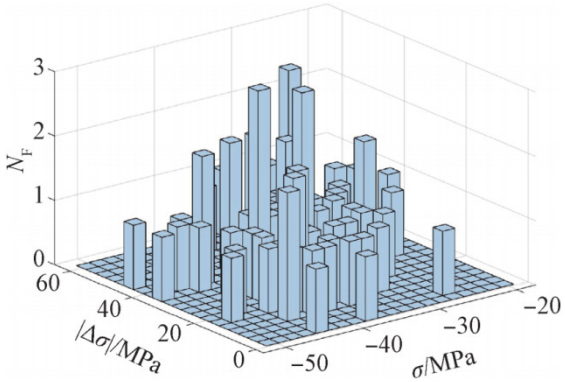

Figure 20. Rain-flow counting results of stress time history.

4.3. Fatigue Life and Calculation Process

The stress amplitude obtained using the rain-flow counting method in Section 4.2 does not account for the case when the mean stress is zero. The effect of mean stress on the stress amplitude must therefore be considered and corrected. A commonly used correction method is the Goodman correction [26], which is expressed as:

$$S_0 = \frac{S_a}{1 - S_m / S_u} \tag{1}$$

where S_0 is the corrected stress amplitude, S_a is the original stress amplitude, S_m is the mean stress, and S_u is the material's ultimate tensile strength (620 MPa). After applying the Goodman correction, the corrected stress amplitudes and the corresponding number of stress cycles for each condition were obtained.

The fatigue verification method used in this study is the Miner linear fatigue accumulation theory [27], which assumes that fatigue damage accumulates linearly. For a component subjected to a constant stress level S, the number of load cycles until failure is denoted as N, and the fatigue damage for n cycles is given by:

$$D = n / D \tag{2}$$

The total damage accumulated from different stress levels is the sum of individual damages. The total damage D is calculated as follows:

$$D = \sum_{i=1}^{m} D_i = \sum_{i=1}^{m} \frac{n_i}{N_i} \tag{3}$$

When $D = 1$, the component reaches fatigue failure. The fatigue life of the welded joints is calculated using the *S*-*N* curve of stainless steel S22152, which is calculated as follows:

$$\lg N = -5.08 \lg \Delta\sigma + 15.6388 \quad (4)$$

The joint probability distribution formula for wind speed and wind direction is as follows:

$$f_{\mu,\xi,k}(\theta) = a\theta^5 + b\theta^4 + c\theta^3 + d\theta^2 + e\theta + f \quad (5)$$

where a, b, c, d, e, and f represent the fitting coefficients. Table 4 lists the values of each coefficient for this fifth-order polynomial fit.

Table 4. Fifth-degree polynomial fitting results.

Parameters	*a*	*b*	*c*	*d*	*e*	*f*
$f_\mu(\theta)$	−0.0001	−0.0972	1.3259	−5.6448	7.4024	5.7410
$f_\xi(\theta)$	−0.0022	−0.0014	0.2900	−0.5085	1.8621	1.8446
$f_k(\theta)$	0.0017	−0.0261	0.1339	−0.2521	0.1866	−0.1625

To calculate the joint probability of wind speed and wind direction, the wind speed and wind direction were divided into discrete intervals. In the wind tunnel test, the wind directions were divided into 36 groups with an interval of 10°. For the wind speed, the range of 0–24 m/s was divided into 12 groups, with an interval of 2 m/s. The probability density function was then divided into 12 × 36 sections, and numerical integration was performed for each area to obtain the joint probability density of wind speed and wind direction.

For the fatigue analysis, each rod was also divided into 12 × 36 conditions. Using SAP 2000, the stress time histories were calculated, and the stress amplitude, mean stress, and number of stress cycles were further obtained using the rain-flow counting method. For each condition, the cumulative fatigue damage was calculated using the Miner formula. The cumulative damage was then multiplied by the probability of each condition's occurrence. The results for all 12 × 36 conditions were summed to obtain the total cumulative fatigue damage for a single rod within 1 min. This value was then multiplied by 60 × 24 × 365 to obtain the annual cumulative fatigue damage, and the reciprocal of this value was taken to calculate the fatigue life. Based on these steps, the fatigue life for the four rod connection nodes was obtained, as shown in Table 5. It is evident that the most unfavorable fatigue life is 380 years, during which no fatigue damage occurs.

Table 5. Fatigue life at node connections of members.

Member Number	72	103	111	126
Lifespan/a	628	511	380	902

5. Conclusions

This study focuses on the design, material selection, and fatigue analysis of a dynamic movable sculpture at the top of the Welcome Tower in Yazhou Bay Bougainvillea Park, Sanya. The sculpture, driven by mechanical systems, consists of eight movable leaves that transform into five distinct shapes. The design addresses the challenges of the harsh coastal environment by using nickel-saving stainless steel (S22152/S32001), chosen for its durability and corrosion resistance. A comprehensive mechanical system enables the leaves to perform functions such as rising, opening and closing, and rotating, all driven by a hydraulic system. To withstand wind loads, the sculpture incorporates safety

mechanisms, including horizontal safety rods and locking devices for added stability in high wind conditions.

The fatigue analysis of the sculpture was conducted using wind tunnel test data, numerical simulations, and the rain-flow counting method. The study found that the maximum stress at the ball joints, where the rods are connected, was approximately 1.5 times that of the individual rods. The Goodman correction was applied to adjust the stress amplitude for mean stress effects, and the Miner linear fatigue accumulation theory was used to calculate the fatigue damage. The analysis revealed that the most unfavorable fatigue life for the sculpture's components is 380 years, indicating that the structure will not experience fatigue damage during its expected lifespan. This research provides valuable insights into the design and material selection for dynamic sculptures in coastal environments, ensuring their long-term stability and resilience to wind-induced fatigue.

Author Contributions: Conceptualization, L.G. and H.L.; Methodology, L.G.; Software, M.R. and L.J.; Validation, L.G., H.L., H.W., and J.C. (Jianguo Cai); Formal analysis, L.G., H.L., M.R., L.J., J.C. (Jie Chen) and D.D.; Investigation, L.G., H.L., M.R., L.J., J.C. (Jie Chen), D.D., H.W., and J.C. (Jianguo Cai); Resources, H.L., H.W., and J.C. (Jianguo Cai); Data curation, L.G.; Writing—original draft preparation, L.G.; Writing—review and editing, H.L., M.R., and H.W.; Visualization, M.R., L.J., and J.C. (Jie Chen); Supervision, L.J.; Project administration, H.L. and D.D.; Funding acquisition, L.G. and J.C. (Jianguo Cai). All authors have read and agreed to the published version of the manuscript.

Funding: The work presented in this article was supported by the National Key Research and Development Program of China (2021YFB3802000, 2021YFB3802005), the Fundamental Research Funds for the Central Universities (2242024K30020, 2242023K40038), the National Natural Science Foundation of China (U22B2092), and the Shanghai Rising-Star Program (23QB1400700).

Data Availability Statement: The raw data supporting the conclusions of this article will be made available by the authors on request.

Conflicts of Interest: The authors declare that they have no known competing financial interests or personal relationships that could have appeared to influence the work reported in this paper.

References

1. Cuong, T.-H.; Kim, J.; Shin, J.; Lee, D.H.; Kim, S.; Lee, K. Effects of fatigue behavior on the performance of composite UHPC panel under high and low-cycle wind loads. *Constr. Build. Mater.* **2024**, *456*, 139188. [CrossRef]
2. Yu, H. Key Technologies for Anticorrosion and Reinforcement of Coastal Building Structures in Alkaline Environment. *J. Coast. Res.* **2020**, *110*, 239–242. [CrossRef]
3. Ye, X.; Bastidas-Arteaga, E.; Li, Q. Reliability-based conformity control method for chloride diffusivity of coastal reinforced concrete buildings. *J. Build. Eng.* **2024**, *87*, 108997. [CrossRef]
4. Wang, L.; Wu, S.; Pei, J.; Meng, X. Dual-Domain Synergistic Optimization for Dynamic Reliability Enhancement of Towering Structures in Nonstationary Wind Fields. *Appl. Sci.* **2025**, *15*, 6670. [CrossRef]
5. Zhang, Y.; Meng, Q.; Li, C.; Ren, P.; Wang, J. Effect of salt on thermal properties of natural stone curtain wall materials: A case study of red sandstone. *J. Build. Eng.* **2025**, *102*, 111977. [CrossRef]
6. Cook, M.; Bouchette, F.; Mohammadi, B.; Sprunck, L.; Fraysse, N. Optimal Port Design Minimizing Standing Waves with A Posteriori Long Term Shoreline Sustainability Analysis. *China Ocean Eng.* **2021**, *35*, 802–813. [CrossRef]
7. Ke, S.; Wang, T.; Ge, Y.; Wang, H. Wind-induced fatigue of large HAWT coupled tower–blade structures considering aeroelastic and yaw effects. *Struct. Des. Tall Spec. Build.* **2018**, *27*, e1467. [CrossRef]
8. Li, J.-X.; Wang, L.-P.; Zhang, Z.-Q.; Zhang, C.; Dong, Z.-Q. Fragility analysis of wind turbine towers under combined wind and seismic loads considering wind-induced fatigue. *Eng. Fail. Anal.* **2025**, *174*, 109472. [CrossRef]
9. Li, Y.; Song, Z.; Li, W.; Wei, L.; Tian, G.; Hu, H.; Dong, X.; Cheng, G.; Feng, X.; Ding, J. Durable Superhydrophobic Bilayer Coating for Carbon Steel with Integrated Corrosion Resistance and Anti-icing Performance. *Langmuir* **2025**, *41*, 25037–25048. [CrossRef]
10. Song, D.; Wang, J.; Guan, H.; Zhang, S.; Zhou, Z.; Zhang, S. Enhanced Corrosion Resistance of Carbon Steel Rebar in Chloride-Containing Water Solutions: The Role of Lotus Extract in Corrosion Inhibition. *Metals* **2025**, *15*, 510. [CrossRef]
11. Tang, Y.; Zhao, J.; Si, Y.; Li, K.; Zhang, L.; Zhao, L.; Li, S.; Wen, T.; Cao, P. Effect of Controlled Rolling on the Strength and Toughness of Low-Alloy Martensitic Steel. *Steel Res. Int.* **2024**, *95*, 2300409. [CrossRef]

12. Senthilnathan, G.; Ayyadurai, G.K.; Jayaprakash, R.; Preethi, B.; Purushothaman, R.; Rani, S.K. Anti-corrosive efficacy of indanyl methacrylate copolymers ratio on mild steel in salt water and DFT investigations. *Iran. Polym. J.* **2025**, *34*, 947–962. [CrossRef]
13. Pei, W.; Yang, S.; Cao, K.; Zhao, A. Effect of Annealing Temperature on Mechanical Properties and Work Hardening of Nickel-Saving Stainless Steel. *Materials* **2023**, *16*, 3988. [CrossRef] [PubMed]
14. Tian, H.; Chu, M.; Pan, J.; Zhu, D.; Yang, C.; Tang, J. Smelting characteristics of nickel-chromium-manganese bearing prereduced pellets for the preparation of nickel saving austenite stainless steel master alloys. *Powder Technol.* **2024**, *441*, 119862. [CrossRef]
15. Liu, T.; Lin, Y.; Zheng, K.; Wang, H.; Zheng, Z. Effect of minor Zr on oxidation resistance and mechanical property of nickel-saving austenitic heat-resistant cast steel. *Mater. Res. Express* **2019**, *7*, 016514. [CrossRef]
16. Mao, L.Y.; Luo, Z.A.; Huang, C.; Wang, Y.Q.; Duan, R.H.; Zhang, X.M. Effects of grain boundary character distribution on hydrogen-induced cracks initiation and propagation at different strain rates in a nickel-saving and high-nitrogen austenitic stainless steel. *Mater. Sci. Eng. A* **2023**, *862*, 144509. [CrossRef]
17. Garrison, C.E.; Price, K.A.; Field, E.K. Environmental Evidence for and Genomic Insight into the Preference of Iron-Oxidizing Bacteria for More-Corrosion-Resistant Stainless Steel at Higher Salinities. *Appl. Environ. Microbiol.* **2019**, *85*, e00483-19. [CrossRef]
18. Kappenthuler, S.; Seeger, S. Holistic evaluation of the suitability of metal alloys for sustainable marine construction from a technical, economic and availability perspective. *Ocean Eng.* **2021**, *219*, 108378. [CrossRef]
19. Chu, H.; Guan, Y.; Zhai, J.; Chen, F.; Lin, J. Corrosion fatigue damage and mechanism evolution of Q420B steel in simulated dry/wet cyclic coastal atmosphere. *Mater. Sci. Eng. A* **2025**, *919*, 147515. [CrossRef]
20. Ma, H.; Deng, Y.; Chang, X. Effect of long-term lateral cyclic loading on the dynamic response and fatigue life of monopile-supported offshore wind turbines. *Mar. Struct.* **2024**, *93*, 103521. [CrossRef]
21. Williams, S.A.; Pelecanos, L.; Darby, A.P. A practical two-parameter model of pile–soil gapping for prediction of monopile offshore wind turbine dynamics. *Géotechnique* **2022**, *74*, 265–280. [CrossRef]
22. Zhou, W.; Guo, Z.; Wang, L.; Rui, S. Dynamic Responses of Jacket Foundation Offshore Wind Turbine Considering the Cyclic Loading Effects. In Proceedings of the Energy Geotechnics, Taipei, China, 14–18 October 2019; Ferrari, A., Laloui, L., Eds.; Springer International Publishing: Cham, Switzerland, 2019; pp. 451–458.
23. Lin, K.; Wei, X.; Zhou, A. Experimental investigation of seismic responses in monopile-supported wind turbines considering operational history using integrated wind tunnel and shaking table testing. *Ocean Eng.* **2025**, *341*, 122783. [CrossRef]
24. Huang, A.; Chen, J.; Song, J.; Chang, J.; Liu, Y. Research Progress of Economic Type Duplex Stainless Steel Welding. *Hot Work. Technol. Chin.* **2016**, *45*, 7–10, 6. [CrossRef]
25. Yan, C.; Zhuo, N.; Gao, Z. Rainfall-Runoff Real-Time Counting Model. *J. Beijing Univ. Aeronaut. Astronaut. Chin.* **1998**, *24*, 623–624.
26. Gui, H.; Li, Z.; Zhang, C.; Liu, H.; Li, S.; Tuo, L.; Wen, J.; Li, Q.; Shen, C. Study on fatigue life of straightening roller based on Miner theory. *J. Plast. Eng. Chin.* **2024**, *31*, 215–221.
27. Yang, X.; Yao, W.; Duan, C. The Review of Ascertainable Fatigue Cumulative Damage Rule. *Strateg. Study CAE Chin.* **2003**, *5*, 81–87.

Disclaimer/Publisher's Note: The statements, opinions and data contained in all publications are solely those of the individual author(s) and contributor(s) and not of MDPI and/or the editor(s). MDPI and/or the editor(s) disclaim responsibility for any injury to people or property resulting from any ideas, methods, instructions or products referred to in the content.